

Modelling of Thermal Quantities for Quick Process Assessment and Process Capability Space Refinement at an Early Design Phase During Laser Welding

Anand Mohan (✉ a.mohan.2@warwick.ac.uk)

University of Warwick <https://orcid.org/0000-0002-8720-2777>

Dariusz Ceglarek

University of Warwick

Michael Auinger

University of Warwick

Research Article

Keywords: Laser welding, Beam oscillation, Heat transfer, Thermal profile, Cooling rate, Process capability space.

Posted Date: December 8th, 2021

DOI: <https://doi.org/10.21203/rs.3.rs-1129775/v1>

License: © ⓘ This work is licensed under a Creative Commons Attribution 4.0 International License.

[Read Full License](#)

Modelling of thermal quantities for quick process assessment and process capability space refinement at an early design phase during laser welding

Anand Mohan, Dariusz Ceglarek, Michael Auinger

Warwick Manufacturing Group (WMG), University of Warwick, Coventry, CV4 7AL, UK

E-mail: a.mohan.2@warwick.ac.uk, d.j.ceglarek@warwick.ac.uk,
m.auinger@warwick.ac.uk.

Abstract:

This research aims at understanding the impact of welding process parameters and beam oscillation on the weld thermal cycle during laser welding. A three-dimensional heat transfer model is developed to simulate the welding process, based on the finite element (FE) method. The calculated thermal cycle and weld morphology are in good agreement with experimental results from literature. By utilizing the developed heat transfer model, the effect of welding process parameters such as heat source power, welding speed, radius of oscillation, and frequency of oscillation on the intermediate performance indicators (IPIs) such as peak temperature, heat-affected zone volume (HAZ), and cooling rate is quantified. Parametric contour maps for peak temperature, HAZ volume, and cooling rate are developed for the estimation of the process capability space. An integrated approach for rapid process assessment, process capability space refinement, based on IPIs is proposed. The process capability space will guide the identification of the initial welding process parameters window and help in reducing the number of experiments required by refining the feasible region of process parameters based on the interactions with the IPIs. Here, the peak temperature indicates the mode of welding performed while the HAZ volume and cooling rate are weld quality indicators. The regression relationship between the welding process parameters and the IPIs is established for quick estimation of IPIs to replace time-consuming numerical simulations. The proposed approach provides a unique ability to simulate the laser welding process and provides a robust range of process parameters.

Keywords:

Laser welding, Beam oscillation, Heat transfer, Thermal profile, Cooling rate, Process capability space.

1. Introduction

Current environmental regulations and policies aimed at reducing carbon emissions have accelerated the need to develop industry capabilities for a higher uptake of lightweight structures for e-mobility and fuel efficiency [1, 2]. In turn, these requirements have led to the development of joining processes with capabilities for: (1) joining multi-material [3, 4]; (2) high welding speed for high volume manufacturing of multiple product variants; and, (3) rapid development and deployment of new joining processes as required by shortened lead time and increased product variants [5]. Remote Laser Welding (RLW) is one of the joining processes which can potentially meet the aforementioned requirements due to several advantages such as imposing heat in a very controlled manner by modulating power and location of the heat source which provides flexibility in terms of thermal cycle developed. It provides flexibility and control over process parameters and other process variables like beam oscillation to deliver heat to the needed area of the workpiece. It offers a non-contact single-sided joining technology that allows high-speed welding for high volume manufacturing [6]. However, a key challenge is shortening the new process development and selection of key process parameters to meet welding thermal outputs pertaining to weld quality. Currently, the development of the RLW process is time-consuming due to the interactions between those factors that provide flexibility. Consequently, process development at present has relied on physical experimentations. Since modelling of weld thermal cycle, is becoming more advanced, there is an opportunity to augment some of the physical experimentation through computer simulations.

The heat-treatment induced during the welding thermal cycle causes significant metallurgical changes to the surroundings of the weld area (heat affected zone, HAZ) which determines the quality and mechanical properties of the weld. Therefore, the understanding and selection of the welding thermal cycle is a crucial task in obtaining desired weld quality as described by microstructure and mechanical properties. To be able to do this, it is important to model the relations between welding thermal cycle; welding process parameters (WPPs); and welding thermal outputs. It is worth noting that these relations are crucial not only to select WPPs but also to estimate welding process capability, to understand process variation and then be able to control the process during the production phase. In the case of RLW, the key WPPs which govern the local temperature distribution during the weld thermal cycle are welding speed,

heat source power modulation and beam oscillation [6]. These WPPs are highly coupled with varying sensitivity to IPIs. For example, the adjustment of beam oscillation modifies the weld thermal cycle and results in changes of weld IPIs such as the peak temperature, HAZ volume and cooling rate which affects the weld microstructure and the mechanical properties [7, 8].

Overall, there is a strong need for both welding process parameter selection and understanding their sensitivity to IPIs that need to be determined during the process design phase ideally via simulations or with a minimum number of physical experiments. Physical experiments alone are not sufficient to survey the entire design space, as it takes weeks or months to run them. Efficient simulation of weld thermal cycle provides option to be (i) run in the entire parameters space (high fidelity simulations which replace physical experimentations); or (ii) integrated with physical experiments in such a way that simulations are run in un-tested settings of parameters space decreasing the number of experiments required (lower fidelity simulations which reduce the number of physical experiments). Experimental measurements of peak temperature and cooling rate are difficult due to very high peak temperature and small weld pool formed, however, they can be quantified by using simulation and modelling tools [9].

The local temperature distribution during the weld thermal cycle is important for process assessment. Moreover, with the advent of high computational advancements, numerical approaches such as finite element (FE) methods have gained importance as these can model different material combinations, heat source types, geometrical configuration, and boundary conditions for laser welding. The state of the art for numerical simulation of the welding processes can be found in [10–12]. To evaluate the thermal cycle, a precise elucidation of the heat source is crucial. Several heat transfer models have been developed for different dimensions and shapes of the heat source for the determination of the thermal cycle, by setting appropriate energy balance. Rosenthal *et al.* [13, 14] proposed a point heat source moving in an infinite material and Hook *et al.* [15] approximated the solution to predict power needed to cause melting. Various one-dimensional and two-dimensional heat source models have been developed considering that the keyhole formed is circular and isothermal [16–18]. Heat transfer models with several designs of the heat source(s) from the very basic cylindrical to the most realistic conical/elliptical, double ellipsoidal or the combination of them are developed [19–21]. A numerical model for the three-dimensional (3D) transient heat source to calculate the temperature distribution is developed for full and partial penetration during welding [22–25]. Bianco *et al.* [28] showed that a quasi-steady state of the

temperature profile is reached and Shanmugan *et al.* [27, 28] consider the heat source as a 3D conical Gaussian heat source to calculate the distribution of temperature in the laser-welded T-joint. The Gaussian distribution is one of the most used methods to describe the continuous heat distribution from the laser beam [29]. However, only a few studies have addressed the modelling of beam oscillation and its interactions on the weld thermal cycle, but the interest is on the rise.

In welding simulation, inputs are understood as welding process parameters (WPPs) and the quality performance is evaluated by using multiple outputs which are called Intermediate Performance Indicators (IPIs) in this paper. It was observed that these process parameters not only affect the welding thermal cycle IPIs, but also the key performance indicators of other downstream processes. However, the current literature has focussed mainly on single or multiple inputs and single-output scenarios which are not sufficient as laser welding is characterised as multiple inputs and multiple outputs (MIMO) [30]. In this paper, a comprehensive and detailed process variation has been performed and addresses the MIMO scenario. To the best of our knowledge, there are not many conclusive studies reported in the literature so far which describe the interactions between the welding speed, heat source power and beam oscillation.

In addition to the existing numerical models, it is needed to study the effect of beam oscillation on the weld thermal cycle. For this reason, this paper introduces a simulation methodology to develop (i) a numerical model for the welding process and design space refinement considering multiple inputs (*i.e.* key WPPs) and multiple-outputs (*i.e.* IPIs) system by conducting computer simulations; (ii) process capability space (Pc-space) depicted by parametric contour maps based on the developed numerical model that allows the estimation of a desired process fallout rate in the case of violation of process; and, (iii) a surrogate model to develop the relationship between the WPPs and IPIs and also for the quick estimation of IPIs without running time-consuming numerical simulations. The Pc-space is the subset of the design space which includes all the selected WPPs producing all the accepted IPIs. The proposed methodology provides a unique ability to: (1) simulate the effect of process variation as generated by the manufacturing process; (2) generate the relationship between the WPPs and the IPIs and assess the sensitivity of process parameters on the IPIs; and (3) design space refinement under quality requirements.

2. Modelling Approach

The approach proposed in this study addresses two main limitations of the current literature as mentioned in the introduction section by taking into consideration (i) oscillating beam as a process parameter for modelling welding cycle, (ii) MIMO scenario, and (iii) process variation over the design space to reduce the number of physical experimentations required. The Pc-space is defined to address the limitations by establishing a set of IPIs to extensively evaluate the laser welding process and refinement of the design space based on the given quality requirements. The flowchart of the three main objectives in this study are: (i) weld thermal cycle estimation; (ii) process capability space definition and visualization; (iii) process parameters selection which is shown in Figure 1 along with the necessary sub-steps.

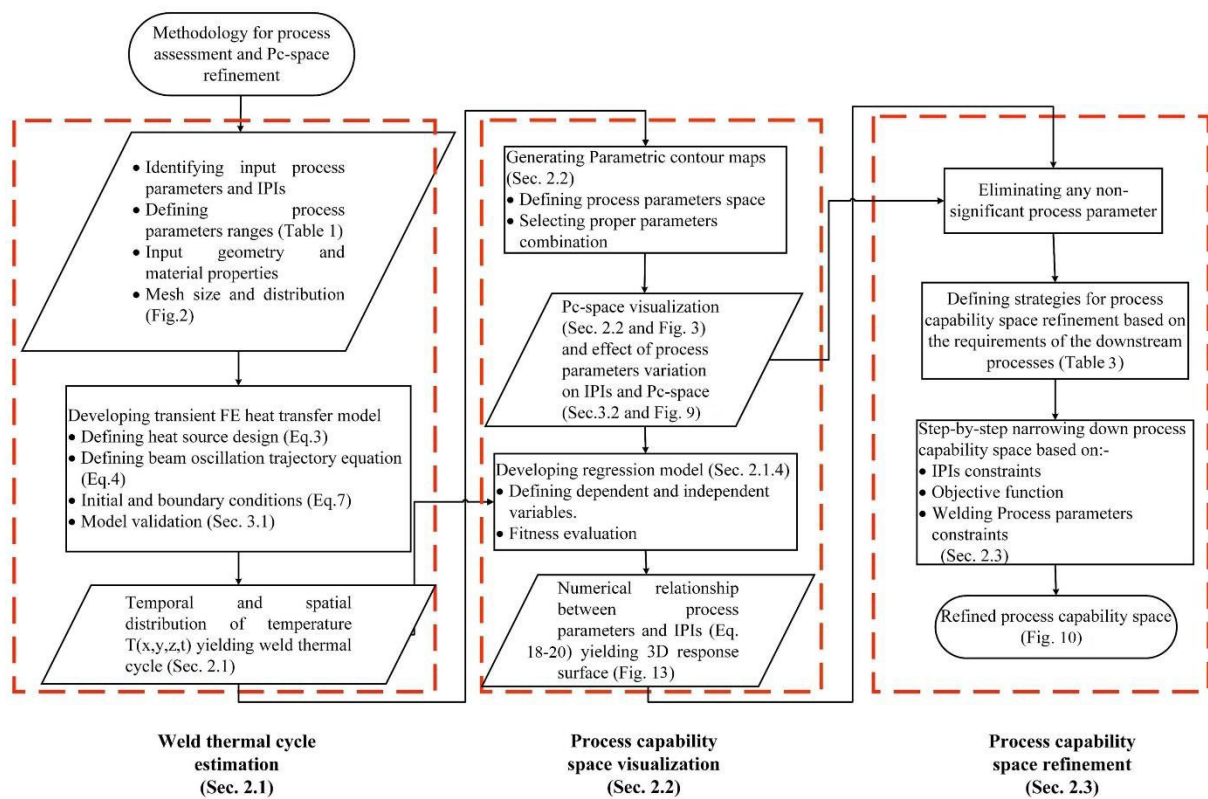


Fig. 1 Flowchart of the main objectives of this study along with necessary sub-steps and mentioning respective sections, figures, tables, and equations used in the paper.

2.1 Transient FEM heat transfer model for weld thermal cycle estimation

The first objective of this study is to estimate the weld thermal cycle using a transient heat transfer model which enables to calculate the spatial and temporal distribution of temperature ($T(x,y,z,t)$) during welding. The geometry with the mesh element size and distribution is shown in Figure 2. To simplify the calculations, several assumptions were considered for developing the model. A Gaussian distributed heat source was considered and assumed

perpendicular to the surface of the workpiece. No gap between the two metal plates was considered. Material properties such as thermal conductivity (k), heat capacity (c_p) and density (ρ) were assumed to be temperature dependent. No convection in the melt pool was considered in the model. Additional contributions to the calculated temperature profile as originating from oxidation (i.e., exothermal reactions) and local effects of the shielding gas near the melt pool were not considered in this research work.

2.1.1 Geometry

A 3D Cartesian coordinate system is used. The heat source is moving in the x -direction and it is incident in the z -direction at $z = 0$. In the 3D model, the size of the plate was 100 mm \times 50 mm with a thickness of 3 mm. For the better mesh distribution near the weld centre line, each plate was divided into three domains having dimensions 100 mm \times 49 mm \times 3 mm, 100 mm \times 1 mm \times 3 mm and 100 mm \times 1 mm \times 3 mm, respectively. The tetrahedral mesh design was used for the simulation. For the validation of the model, material properties and geometry was following Sonia *et al.* [31] having a dimension of each plate as 100 mm \times 50 mm with a thickness of 2 mm for the Titanium alloy and 3 mm for the Aluminium alloy. The material properties are reported in Table A.1 and Table A.2 in the Appendix A. In this study, the materials used for generating results are Aluminium 6061 alloy and Aluminium 5754 alloy. Finite element mesh consisted of about 1169117 domain elements, 102412 boundary elements and 4528 edge elements having higher density near the fusion zone (FZ) and HAZ as compared to the rest of the structure.

2.1.2 Governing Equations

The heat source is considered striking normally to the work-piece surface, along the z -axis and moving with constant welding speed in the x -axis. The time-dependent temperature field is a function of position (x, y, z) and time (t) which is determined by the non-linear energy conservation Eq. (1) [32].

$$\rho c_p \left[\frac{\partial T}{\partial t} \right] = \vec{\nabla} \cdot (k \vec{\nabla} T) + Q_{laser} \quad (1)$$

Where ρ (kg m⁻³) is the material density, c_p (J kg⁻¹ K⁻¹) is the specific heat capacity of the material, T (K) is the temperature of the workpiece, t (s) is the time, k (W m⁻¹ K⁻¹) is the thermal conductivity of the material, and Q_{laser} (J m⁻³) is the energy input of the laser heat source. The phase changes are considered to include temperature change due to latent heats

by using the apparent heat capacity method which includes an additional term for latent heat as shown in Eq. (2)

$$C_P = C_{P,solid} \cdot (1 - f_l) + C_{P,liquid} \cdot f_l + L_{s \rightarrow l} \frac{\Delta f_l}{\Delta T} H_m \quad (2)$$

Where, $C_{p,solid}$ is the heat capacity of the solid phase, $C_{p,liquid}$ is the heat capacity of the liquid phase, $L_{s \rightarrow l}$ is the latent heat and f_l is the phase transition function. For pure solid $f_l = 0$, and for pure liquid $f_l = 1$.

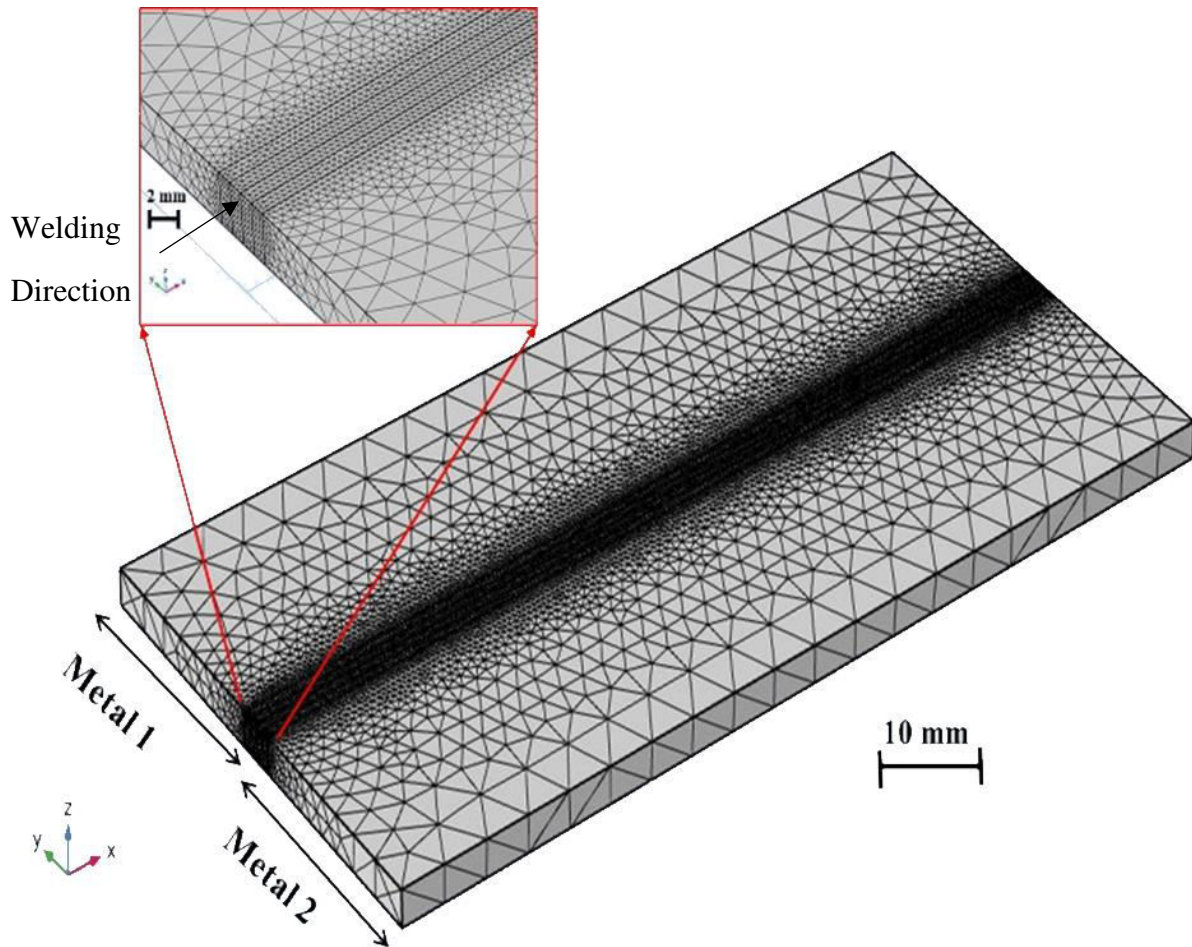


Fig. 2 Schematic illustrations of finite element mesh size and mesh distribution used for the simulations.

2.1.3 Heat source design and boundary conditions

A 3D cylindrical and conical volumetric heat sources are the most used heat source designs for the modelling of thermal quantities during laser welding [18, 33]. It has gaussian-shaped energy distribution, and the maxima are at the nominal power of the heat source. A 3D conical heat source with origin (x_0, y_0, z_0) is defined by a Gaussian distribution as shown in Eq.

(3). Note that this relationship represents the 3σ range (99.7% of total heat input) of a heat source with radius r and penetration depth d [34].

$$Q(x, y, z) = \frac{3P}{\pi r^2 d} \exp\left(-3 \frac{(x-x_0)^2 + (y-y_0)^2}{r^2}\right) \exp\left(-3 \frac{(z-z_0)^2}{d^2}\right) \quad (3)$$

Where, P (W) is the power of the heat source beam, r (mm) is the heat source spot radius, d (mm) is the maximum depth of penetration. In the conical design of the heat source, the temperature is maximum at the surface and minimum at the bottom which is a simplified representation of the keyhole formation during laser welding. To define the moving heat source, the position of its centre needs to change with time. Hence, we write $(x(t), y(t), z(t))$ for the position of the heat source centre at time t . The position at the start of the simulation ($t=0$) was chosen to be at the origin (x_0, y_0, z_0) .

The derived trajectory of an oscillated heat source is considered to be at the surface, starting at the point connecting the two plates for welding ($z(t) = z_0$). Circular oscillated heat sources in the xy -plane are used because it has been found that less welding defects were observed experimentally [12, 35, 36]. The trajectory of the moving heat source is defined by Eq. (4)

$$(x(t), y(t), z(t)) = (x_0 + St - R(1 - \cos(2\pi ft)), y_0 + R\sin(2\pi ft), z_0) \quad (4)$$

Where $x(t)$, $y(t)$ and $z(t)$ are time-dependent heat source spot coordinates, x_0 , y_0 and z_0 mark the initial position of the heat source, S (mm min^{-1}) is the welding speed, R (mm) is the radius of oscillation, f (Hz) is the oscillation frequency and t is the time. The term St gives the displacement in the welding direction while $(1 - R\cos(2\pi ft))$ and $R\sin(2\pi ft)$ produce the circular rotation for the oscillation of the beam. In Eq. (4) at $R = 0$ and $f = 0$ gives the equation of no oscillation condition. The term $Q_{laser}(x, y, z, t)$ is the moving heat source term in the energy conservation equation (Eq. (1)). The expression for $Q_{laser}(x, y, z, t)$ can be defined by inserting the coordinates of the spot centre from Eq. (4) into Eq. (3) leading to the relation as shown in Eq. (5).

$$Q_{laser}(x, y, z, t) = \eta \frac{P}{\pi r^2 d} \exp\left(-3 \frac{(x-x(t))^2 + (y-y(t))^2}{r^2}\right) \exp\left(-3 \frac{(z-z(t))^2}{d^2}\right) \quad (5)$$

Where P is the nominal power of the heat source beam, r is the spot radius and d is the penetration depth and x, y, z is the position of the point where the temperature is calculated, η is the absorption coefficient of material and defined by Eq. (6) [37]

$$\eta(T) = 0.365 \left(\frac{\alpha}{\lambda}\right)^{1/2} - 0.0667 \left(\frac{\alpha}{\lambda}\right) + 0.06 \left(\frac{\alpha}{\lambda}\right)^{3/2} \quad (6)$$

where α is the electrical resistivity of the workpiece and λ is the wavelength of the laser. Eq. (5) represents the heat input by the moving conical heat source with and without beam oscillation. The initial temperature of the workpiece is assumed to be maintained at room temperature (T_0). The energy absorbed by the workpiece is transferred by conduction, which further is partially lost due to the contact with the ambient atmosphere and by radiation leading to cooling. The heat loss due to the contact with the ambient atmosphere and by radiation during welding are governed by Newton's law of cooling and Stefan-Boltzmann relation [38]. Convective and radiative heat loss is considered for the top and bottom surfaces which follows Eq. (7)

$$-k\nabla T = h(T - T_0) + \varepsilon\sigma(T^4 - T_0^4) \quad (7)$$

The governing energy conservation equation is discretized using the finite element method. The solution to the above energy conservation equation gives the spatial and temporal distribution of the temperature yielding weld thermal cycle. The input process parameters are welding speed, heat source power, radius of oscillation, frequency of oscillation and heat source spot size as depicted in Eq. (4) and Eq. (5). The peak temperature, HAZ volume and cooling rate is calculated from the weld thermal cycles as the outputs.

2.1.4 Formulation of Surrogate Model for regression relation between WPPs and IPIs

A surrogate model is developed to formulate an analytical relationship between the WPPs and the IPIs using a second order and third-order polynomial expression. The linear expression is not sufficient to model a non-linear complex relationship whereas higher-order polynomial expressions would lead to over-fitting. The general formulation of the second order and third-order polynomial expressions is shown in Eq. (8).

$$y = \beta_0 + \sum_{i=1}^k \beta_i x_i + \sum_{i=1}^k \left(\sum_{j=1}^i \beta_{ij} x_i x_j \right) + \sum_{i=1}^k \sum_{j=1}^i \left(\sum_{l=1}^i \beta_{ijl} x_i x_j x_l \right) \quad (8)$$

Where x_1, x_2, \dots, x_k are independent variables and $\beta_0, \beta_i, \beta_{ij}, \beta_{ijl} \dots$ are the regression coefficients. The regression model is developed by writing codes in Python. The coefficient of determination (R-square) is calculated and t-test, p-value were evaluated to assess the goodness of surrogate models. The dispersion between the predicted and measured values was plotted to visualize the closeness in the prediction to the actual value from the numerical

model. R-square depicts the goodness and relative measure of fit. To evaluate the significance of regression coefficients t-statistics and p-value are calculated with a 95% confidence interval. A 10-Fold Cross Validation has been performed to assess the predictive performance of the surrogate model. A 10-Fold R-square is calculated to judge the model performance to new data outside the model data set.

2.2 Process capability space

The quality performance of laser welding is governed by multiple thermal outputs which are called as IPIs in this paper. The input WPPs considered in this study are welding speed (S), heat source power (P), the radius of oscillation (R) and frequency of oscillation (f). The four WPPs (S, P, R, f) are defined in Eq. (9), where i represents the index of WPP, n represents the total number of WPPs.

$$WPPs = \{WPP_i | \forall i = 1, \dots, n\} \quad (9)$$

The upper limits (UL) and lower limits (LL) of input process parameters have been determined by considering technological constraints. These limits were defined by conducting initial welding computer experimentations and physical experimental studies present in the literature, which are not documented in the paper. The upper and lower limits of all the WPPs are given in Table 1. The combination of all possible WPPs within the permitted limits determines design space. In this paper, the design space is represented in the form of parametric contour maps where the x and y -axis show the variation of two different WPPs and the coloured contour surface shows the calculated values of IPIs. The parametric contour maps are developed for three IPIs (1) peak temperature (T_{peak}), (2) HAZ volume (V_{HAZ}) and (3) cooling rate (C_{rate}). The T_{peak} (maximum) is the maximum temperature recorded during welding as given in Eq. (10).

$$T_{peak} = \max(\{T(x, y, z, t)\}) \quad (10)$$

HAZ is a solid portion of the workpiece that undergoes metallurgical transformation due to exposure to the critical temperature ranges during welding. In general, the temperature range for the HAZ is high enough to cause metallurgical transformation, grain growth but not sufficient to melt the metal. This temperature range is calculated using the phase diagram of the alloy. Therefore, the temperature range for the present study is taken between solidus and lower temperature limit where grain growth can be neglected which in this case was very

close to the 933 K-470 K temperature range. The V_{HAZ} was calculated by volumetric integration of the workpiece having HAZ temperature region defined in Eq. (11).

$$V_{HAZ} = \frac{\int_{t_1}^{t_2} \iiint T(x,y,z,t) dx dy dz dt}{\text{number of time steps}}, T \in [470 K, 933 K] \quad (11)$$

The calculated weld thermal cycle is utilised to calculate C_{rate} (dT/dt), which is defined as the change in temperature from the melting point to the 470 K upon the time taken to cool from the melting point to this temperature. The upper and lower limits of the IPIs are given in Table 2. The three IPIs (T_{peak} , V_{HAZ} and C_{rate}) are formulated in Eq. (12-13), where j represents the index of IPI, and m represents the total number of IPIs.

$$IPIs = \{IPI_j | \forall j = 1, \dots, m\} \quad (12)$$

$$IPI_j = f(WPP_1, WPP_2, WPP_3, \dots, WPP_n) \quad (13)$$

Table 1 Welding process parameters and their allowance limits for defining design space.

Welding Process Parameters (WPPs)	WPP ^{LL}	WPP ^{UL}
Speed S (mm min ⁻¹)	1000	6000
Power P (W)	1000	6000
Radius of oscillation R (mm)	0	1.2
Frequency f (Hz)	0	1000

Table 2 IPIs and their allowance limits for defining process capability space.

Intermediate Performance Indicators (IPIs)	IPI ^{LL}	IPI ^{UL}
Peak temperature T_{peak} (K)	933	3500
Cooling rate C_{rate} (K min ⁻¹)	Maximum C_{rate} at LL of T_{peak}	Maximum C_{rate} at UL of T_{peak}
Heat-affected zone volume V_{HAZ} (mm ³)	Minimum V_{HAZ} at LL of T_{peak}	Minimum V_{HAZ} at UL of T_{peak}

The second objective of the work is to develop process capability space. A numerical model is computed to estimate the IPI values over the design space. The model that describes this relationship is given as:

$$\widehat{IPI}_j = M_{IPI_j}(WPP_1, \dots, WPP_n) | \forall j = 1, \dots, m \quad (14)$$

If the estimated IPI violates the allowance limits, WPPs is considered unfeasible. For the j^{th} IPI, process capability space is defined as expressed in Eq. (15), where k is the indices of individual process capability space and m is the total number of IPIs

$$\alpha_j = \begin{cases} \widehat{IPI}_j, & \text{if } IPI_j^{LL} \leq M_{IPI_j}(WPP_1, \dots, WPP_n) \leq IPI_j^{UL} \\ 0, & \text{otherwise} \end{cases} \quad \forall j = \{1, \dots, m\} \quad (15)$$

It defines a set of IPIs which evaluates the laser welding process and identifies the process parameters within the design space satisfying all the quality requirements. The final process capability space is the aggregation of process capability space (α_j) of individual IPI as defined in Eq. (16) and illustrated in Figure 3, where the final image in the upper row (Figure 3(d)) is the intersection of all individual process capability spaces based on the allowance limits of all the IPIs. Figure 3 demonstrates the definition of final process capability space from the design space (Figure 3a) based on the intersection of individual process capability space of each IPIs. The shaded area in yellow represents the feasible region and any process parameters inside this region satisfies all the requirements.

$$Pc - space = \bigcap_{j=1}^m \alpha_j \quad (16)$$

The final process capability space envelops all the feasible WPPs values inside the design space. It provides the estimated feasible range of WPPs which is given as:

$$[\widehat{WPP}_i^{LL}, \widehat{WPP}_i^{UL}] = Pc - space \quad \forall i = 1, \dots, n \quad (17)$$

2.3 Process capability space refinement

The last objective of this study is the refinement of process capability space depending upon the requirements of the downstream processes. This refinement of process capability space can have either of the two objectives: (i) completely replace physical experimentations by providing appropriate process parameters over the entire design space; and, (ii) reduces the number of experiments required by providing IPIs over un-tested settings of design space or refines the initial range of design space to be tested for early design of experiments. It is important to note down that the methodology for process parameters refinement provided in this study are for the early design phase and process assessment.

The process parameters refinement is performed on the final Pc-space. In this work, sequential refinement strategies are developed based on three constraints: (i) IPIs constraints

which address the proper coalescence of metals produced by heating to a suitable temperature; (ii) objective function which addresses the functional and strength requirements to control weld defects and strength of the weld; and, (iii) process parameters constraints which address the key targets of the joining industries to have high production rate, low cost and aesthetic requirements of welded joints. Sequential refinement strategies for some of the downstream processes are given in Table 3 in order of their hierarchy. Welding can be considered as two processes first one is the melting and evaporation of the workpiece to have a fusion and the other is the heat treatment of the workpiece. Both the processes are governed by the thermal cycle applied during welding. Proper control over the thermal cycle applied can improve weld properties or eliminate various weld defects. The IPIs calculated in this study governs the features of the weld thermal cycle and hence can reduce the experimentation required in early design phases.

Table 3 Proposed multiple strategies for process capability space refinement for various downstream processes and requirements.

Target downstream processes requirements	IPIs constraints	Objective function	Welding parameters constraints	Process (WPPs)	Remarks
Improving mechanical properties	$T_{peak}^{UL} \geq T_{peak} \geq T_{peak}^{LL}$	min (V_{HAZ}), max (C_{rate})	$WPP_i^{LL} \leq WPP_i \leq WPP_i^{UL}$ $\forall i = \{1, \dots, N_i\}$ max(S), min(P), $R > 0$		Fine grains formation, uniformly dispersed dendrites (when $R > 0$)
Reducing segregation and intermetallics formation	$T_{peak}^{UL} \geq T_{peak} \geq T_{peak}^{LL}$	max (C_{rate}), min (V_{HAZ}) Stirring using beam oscillation	$WPP_i^{LL} \leq WPP_i \leq WPP_i^{UL}$ $\forall i = \{1, \dots, N_i\}$ max(S), min(P) $R > 0$		Reduces diffusion and improves mixing
Reducing Porosity	$T_{peak}^{UL} \geq T_{peak} \geq T_{peak}^{LL}$	Stirring using beam oscillation max (C_{rate}), min (V_{HAZ})	$R > 0$ $WPP_i^{LL} \leq WPP_i \leq WPP_i^{UL}$ $\forall i = \{1, \dots, N_i\}$ max(S), min(P)		Mechanical stirring by beam oscillation helps in escaping trapped gasses reducing porosity
Partial penetration	$T_{peak}^{UL} \geq T_{peak} \geq T_{bp}$	min (V_{HAZ}), max (C_{rate})	$WPP_i^{LL} \leq WPP_i \leq WPP_i^{UL}$ $\forall i = \{1, \dots, N_i\}$ max(S), min(P)		Partial penetration requires peak temperature above the boiling

				point
--	--	--	--	-------

3. Results and discussion

The transient heat transfer model is validated with the experimental results from the literature. A total number of around 800 numerical simulations were carried out which serve as a base for the discussed results. Each simulation took 25 minutes to solve for no oscillation condition and 105 minutes for oscillation condition. This is due to the increased complexity introduced with the heat source oscillation (Eq. 4) and an increase in the number of mesh elements as the heat source traversing area has been increased. The effect of WPPs on the IPIs and the process capability space has been discussed. The process capability space refinement is illustrated with the help of an example followed by establishing the regression relationship between the WPPs and the IPIs using a surrogate model for the quick estimation of IPIs.

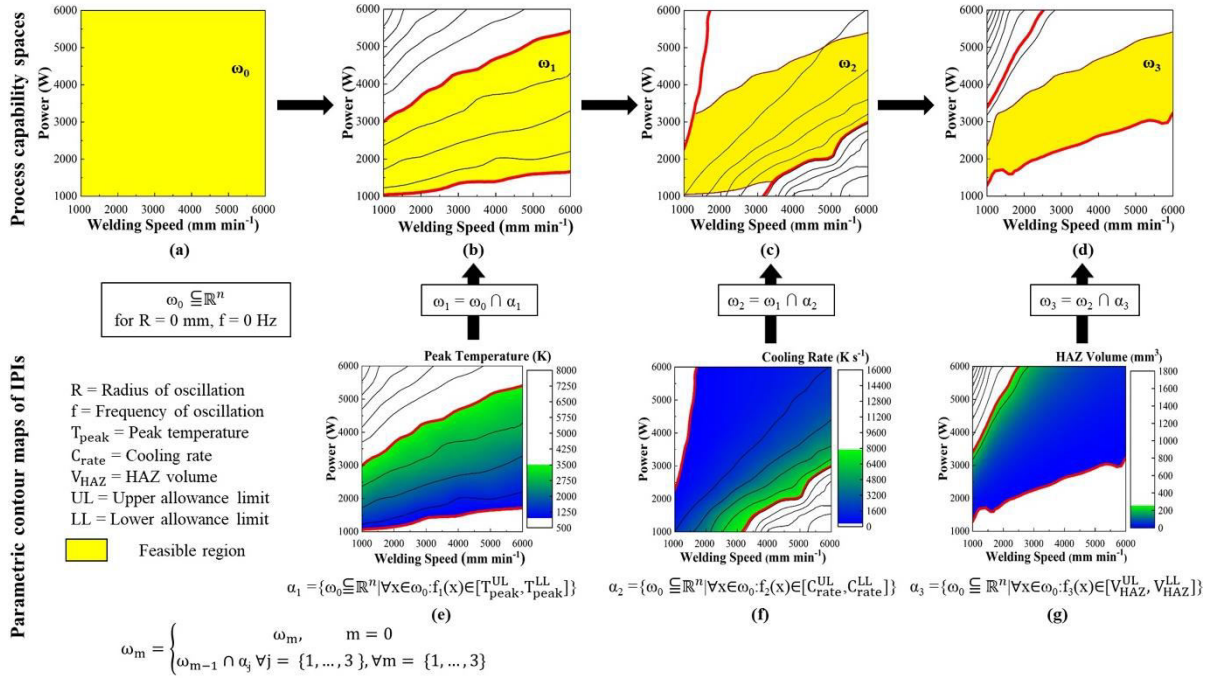


Fig. 3 Conceptual representation of process capability space for no oscillation condition (where $R = 0$ and $f = 0$ Hz). The top row shows the process capability spaces (at each step with an intersection with IPIs) and the bottom row shows the parametric contour maps of each IPIs with the allowance limit.

3.1 Model Validation

The transient heat transfer model is validated by comparing the experimental thermal cycle generated from the thermocouple and the weld morphology from the optical micrographs with the model. The thermal cycle is validated with experimental results reported for the Al-5754 and Ti₆Al₄V alloy systems [31] where an offset of 1 mm was taken along the titanium side and the thermocouple was placed at 2 mm from the welding line on both sides. The thermal cycle generated from the simulation for the validation is at the same position where the thermocouple is placed for recording as shown in Figure 4. The thermal cycle obtained from the simulated model showed a similar tendency to the experimentally obtained thermal cycle from the thermocouple which illustrates the rationality of the numerical model. The obtained values of the peak temperatures were within the acceptable range as the difference is less than 0.1% and is constant throughout the model. The calculated heating cycle is in good agreement with the experimental results having less than the 0.5% difference. While the cooling cycle for both the metals was found to deviate. The discrepancy regarding the cooling cycle is due to the assumption, especially not considering convective heat transfer. The cooling rate calculated from the peak temperature to the minimum temperature was found to deviate by less than 8% for Titanium alloy and less than 2% for Aluminium alloy. This is due to the high thermal conductivity of Aluminium ($158.7 \text{ W m}^{-1} \text{ K}^{-1}$) as compared to Titanium ($14.7 \text{ W m}^{-1} \text{ K}^{-1}$). The weld width is compared from the simulation with the optical micrographs for the laser welded Al-5754 and Al-6061 alloy in butt welding configuration. The optical micrograph, the weld dimensions from the model and the comparison between the experimental and model value for different welding speed is shown in Figure 5. The heat source power is kept constant at 4500 W. The maximum error is 6% and the minimum error is 1.1%. These comparisons show the good agreement between the model and experiments for both calculations related to temperature distribution and weld morphology. To analyse the effect of WPPs on the IPIs and the Pc-space for the welding of Aluminium alloys, the validated numerical model is solved for butt welding of Al-5754 alloy with Al-6061 alloy. The variation of IPIs with varying WPPs is illustrated using parametric contour maps which provides the following types of information: (i) effect of variation of WPPs on the IPIs which can be directly used for the early design of the experiments, (ii) individual Pc-spaces which leads to the final Pc-space for process parameters selection, (iii) existence of multiple paths to achieve the desired IPI, and (iv) effect of beam oscillation on the IPIs during welding as compared to no oscillation condition. Variation of IPIs due to the variation in process parameters are studied for both no-oscillation and beam oscillation conditions.

3.2 Characterization of peak temperature, HAZ volume and cooling rate for no oscillation condition

For the no-oscillation condition, Figure 3(e) shows the simulated peak temperature contours for different combinations of heat source power and welding speed. For laser welding in conduction mode, the peak temperature must remain between the melting and the boiling point of the metal. For the keyhole mode, the peak temperature must be above the boiling point of the metal being welded. In this study, for the full penetration welding, the peak temperature at which the temperature at the bottom surface is just below the melting point leading to full penetration during welding is found to be 3500 K. The upper limit of peak temperature is 3500 K and the lower limit is the melting point to define the process capability space for welding as illustrated in Figure 3(e). The space above the upper peak temperature limit will lead to the cutting of the workpiece and the space below the lower limit will lead to only heating of the workpiece without any melting. The upper and the lower limit of the peak temperature for the process capability spaces can be achieved by multiple possible combinations of process parameters. The cooling rate and HAZ volume are calculated for all these WPPs combinations. The maximum value of the cooling rate is selected from the possible WPPs combination corresponding to the upper limit of the peak temperature. This value is selected as the upper limit of the cooling rate for the Pc-space and similarly, for the lower boundary of the cooling rate, the maximum value is selected from the WPPs combination corresponding to the lower limit of the peak temperature. For the upper and lower limits of HAZ volume for the Pc-space, a minimum value is selected from the possible WPPs combinations corresponding to the upper and lower limit of the peak temperature. The maximum value of the cooling rate and minimum value of HAZ volume is selected because the aim is to maximise the cooling rate and minimise HAZ volume.

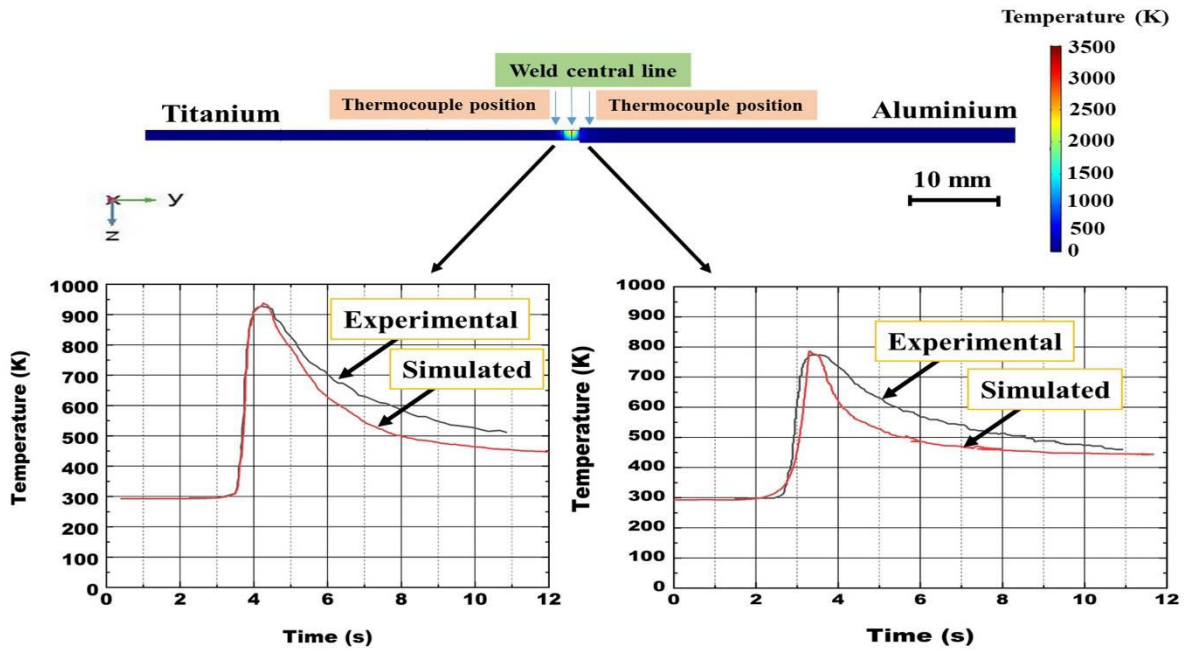


Fig. 4 Calculated temperature distribution of Al-Ti welded joint, investigated in this study (top). The position of the weld central line and the thermocouple (top) is indicated by the arrow (top). Comparison between experimental and simulated thermal cycle at the Titanium (bottom left) and Aluminium side (bottom right). Experimental data has been reproduced from [31].

It was observed that with the increase in power at constant speed the peak temperature increases due to the local increase in net heat input per unit length to the workpiece defined as $(\eta P)/S$. Whereas when the welding speed is increased at constant power, the net heat input to the workpiece decreases, leading to a decrease in peak temperature. The simulated cooling rate and heat-affected zone volume profiles are shown in Figures 3(f) and 3(g), respectively, for different combinations of heat source power and welding speed. It was observed that at constant welding speed with the increase in power HAZ volume increases due to the higher heat input to the workpiece while the cooling rate decreases. Whereas when the welding speed is increased at constant power, the HAZ volume decreases as net heat input to the workpiece decreases, causing a decrease in peak temperature which leads to an increase in cooling rate.

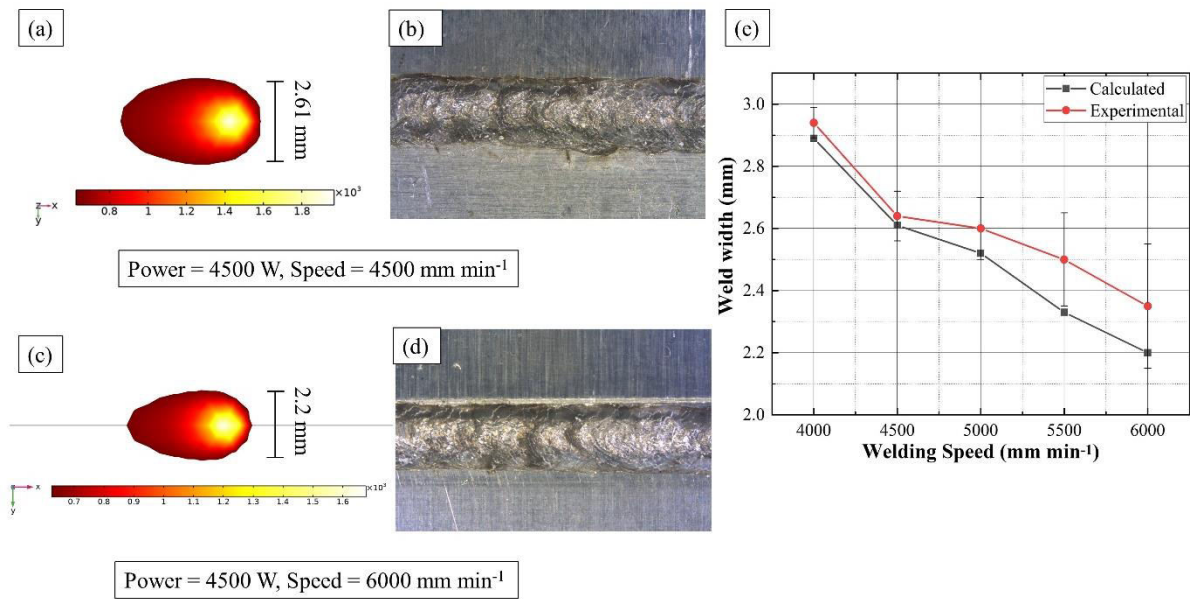


Fig. 5 Comparison between the calculated weld morphology from the model and from the experimented weld optical micrographs for Al-5754 and Al-6061 laser welded joint. Figure (a) shows the calculated weld width, Figure (b) optical micrograph at a heat source power of 4500 W and welding speed of 4500 mm min⁻¹. Figure (c) shows the calculated weld width, Figure (d) optical micrograph at a heat source power of 4500 W and welding speed 6000 mm min⁻¹. Figure (e) shows the comparison between the calculated and experimented value of weld widths for varying welding speed at a constant power of 4500 W.

An important characteristic of the results in Figure 3 is that a particular weld attribute, such as the peak temperature or cooling rate or HAZ volume can be achieved by multiple combinations of welding process parameters. This existence of multiple paths to achieve the desired weld requirements exhibits the flexibility of the laser welding process. For the estimation of Pc-space, the peak temperature is the most important IPI and is chosen first which followed by either of the other two depending upon the requirements of the downstream processes as given in Table 3. The final Pc-space is the intersection of the individual Pc-spaces for all the IPIs as shown in Figure 3(d) and the shape of the final process capability space will remain constant irrespective of the order of IPIs considered.

3.3 Characterization of peak temperature, HAZ volume and cooling rate for beam oscillation condition

Process variables that correspond to the shape and overlapping of the heat source are the radius of oscillation, frequency of oscillation, and welding speed which is explained in detail in Appendix B. Heat input per unit length in case of oscillating heat source is defined as $[(\eta P)/(S + 2\pi Rf)]$. There are two possibilities during circular beam oscillation: (i) no overlapping of the path traversed by the oscillating heat source and, (ii) overlapping of the

path traversed by the oscillating heat source as shown in Figure 14 in Appendix B. The onset of overlapping during oscillating heat source occurs when $(4Rf/S) = 1$ as derived in Appendix B. The term $2\pi Rf$ denotes the circular motion of the oscillating heat source and S denotes the welding speed of the heat source in the welding direction. A higher value of $(2\pi Rf/S)$ implies that the circular motion is more dominant compared to the linear forward motion of non-oscillation welding, leading to more overlapping as shown in Figure 14 (b) and (c). Lower value implies forward motion is dominantly leading to either no overlapping or few overlaps. The number of overlapping points is calculated graphically as explained in Appendix B.

3.3.1 Effect of frequency of oscillation

There are two opposing factors governing heat uptake during oscillating heat source: (i) decrease in heat input per unit length due to increase in effective speed $(S + 2\pi Rf)$ i.e., linear plus circumferential speed and, (ii) increase in heat input due to increase in the number of overlapping points. Figure 6(a) shows the contour plot between the f , ratio of circumferential speed to linear forward speed $(2\pi Rf/S)$ and the heat input per unit length considering overlapping points (calculated in Appendix B). For a constant $(2\pi Rf/S)$, heat input remains constant with the increase in f . It can be inferred from the plot that at a constant value of the $(2\pi Rf/S)$, heat input remains constant with the increase in the frequency of oscillation. This illustrates that the range of frequency, welding speed and radius of oscillation investigated in this study shows that the frequency has a negligible effect on the heat uptake during welding. At a constant frequency, with an increase in the value of $(2\pi Rf/S)$ heat input increases. In this case, the increase in heat input is due to the increase in overlapping points as R increases or decrease in S which leads to an increase in heat input per unit length. This explicit solution is supported by the transient heat transfer simulations as shown in Figure 6. Figures 6(b) and 6(c) show the simulated peak temperature for different combinations of frequency, welding speed and heat source power, it is evident that the effect of frequency of oscillation is negligible on the peak temperature in both cases as contour lines are parallel to the y-axis showing the frequency of oscillation. Similar trends are found for the cooling rate and HAZ volume. With an increase in oscillation frequency, the number of overlapping points for every rotation will increase which leads to re-heating and also the effective speed of the heat source increases as it has to rotate more times in the same amount of time. This re-heating should lead to a rise in temperature, but it is compensated by a decrease in heat energy

absorbed per unit length due to the increase in the actual speed of the heat source. The increase in the actual distance travelled by the heat source with an increase in f is demonstrated in Figure 14 in Appendix B.

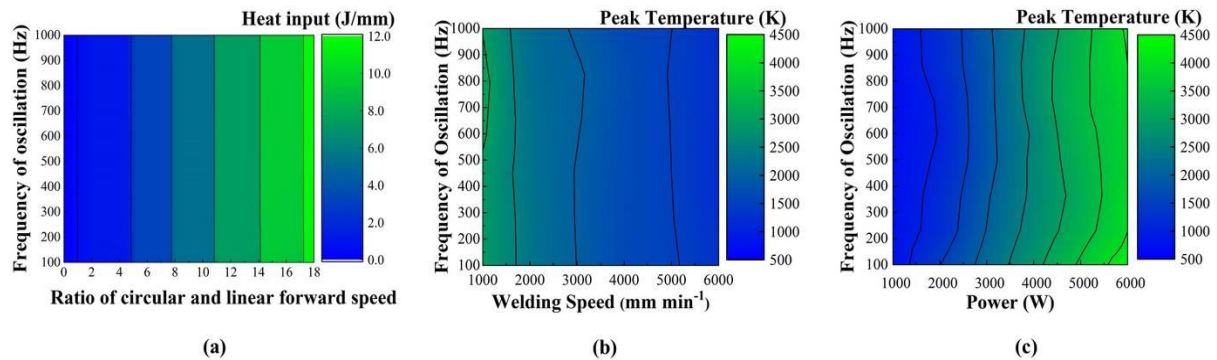


Fig. 6 Heat input per unit length with varying frequency and ratio of circular speed and linear forward speed (welding speed) (a). Figure (b) shows the parametric contour maps for peak temperature depending on the frequency of oscillation and welding speed at a constant power of 3500 W and figure (c) shows the parametric contour maps for peak temperature depending on the frequency of oscillation and heat source power at a constant welding speed of 2500 mm min⁻¹. The oscillation radius R was kept constant at 0.3 mm. The parametric contour maps are developed for the joining of Al-5754 with the Al-6061 alloy system for butt welding configuration.

3.3.2 Effect of the radius of oscillation

To examine the effect of radius of oscillation during laser welding, two types of parametric contour maps are generated: (i) contour maps of IPIs between the radius of oscillation and heat source power at a constant welding speed and frequency of oscillation; and (ii) contour maps of IPIs between the radius of oscillation and the welding speed at a constant heat source power and frequency of oscillation.

Figure 7 shows the simulated parametric contour maps of the peak temperature, HAZ volume and the cooling rate for different combinations of the radius of oscillation and heat source power at a constant welding speed of 2500 mm min⁻¹ and frequency of 200 Hz. As shown in Figure 7(a), at a constant power with an increase in the radius of oscillation, the peak temperature decreases as the effective heat source speed increases which results in the decrease in the heat input per unit length. However, for the HAZ volume, it depends on the relative length of heat source spot radius (r), which is 0.2 mm in this study and the radius of oscillation. When $R \leq r$, the HAZ volume remains constant with the increase in R as it is

equivalent to the situation with a heat source having a larger spot radius. So, an increase in the width of HAZ is compensated by the decrease in depth leading to constant HAZ volume. When $R > r$, there is a sharp decrease in HAZ volume when R is just above r which is depicted in Figure 7(b) at $R = 0.3$ mm. With an increase in R , HAZ volume increases until it reaches $R = 3r$. This is due to the delay in the cooling process due to the repeated heating. Though the maximum value of HAZ volume is still smaller than for $R \leq r$. When $R > 3r$, the heat input rate decreases leading to quick removal of heat which decreases the HAZ volume. So, it can be concluded that HAZ volume decreases with the application of heat source oscillation as in practical cases $R > 2r$. Similarly, the cooling rate remains constant when $R \leq r$, there is a sharp increment when $R > r$ which is shown in Figure 7(c) at $R=0.3$ mm. It again decreases with an increase in R till $R = 3r$. When R is further increased it decreases due to the decrease in heat input rate as the velocity of the heat source increases. At constant power, the lowest cooling rate is found when $R \leq r$. So, the cooling rate increases when beam oscillation is applied (as for practical cases $R > 2r$). A resonance effect is found for the HAZ volume and cooling rate which is a function of oscillation radius and heat source spot size.

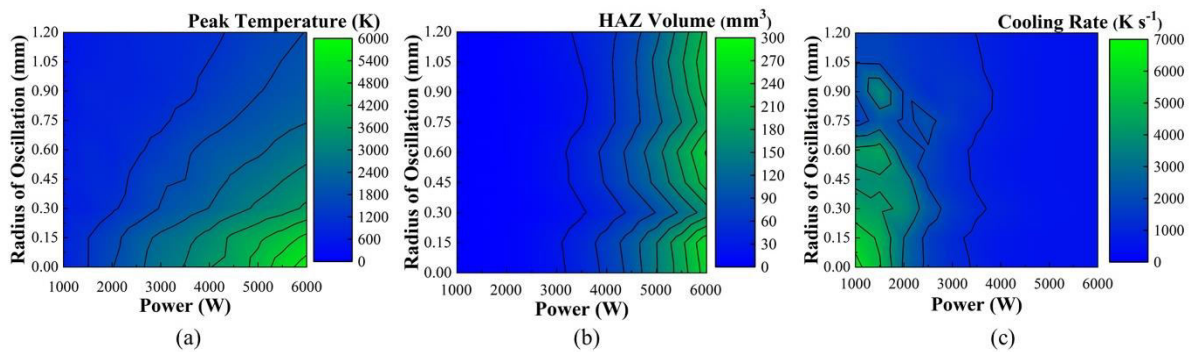


Fig. 7 Parametric contour maps for heat source power vs radius of oscillation at a constant welding speed of 2500 mm min^{-1} , frequency of oscillation of 200 Hz , and spot radius of 0.2 mm . Figure (a) contour maps for peak temperature, (b) contour maps for HAZ volume, and (c) contour maps for cooling rate. The parametric contour maps are developed for the joining of Al-5754 with Al-6061 alloy system for butt welding configuration.

Figure 8 shows the simulated parametric contour maps of the peak temperature, HAZ volume and the cooling rate for different combinations of the radius of oscillation and welding speed at a constant heat source power of 4000 W and frequency of 200 Hz .

The generated parametric contour maps (Figure 8) show similar trends as in Figure 7, but the maxima and minima are exchanged from right to left as both welding speed and heat source power are related to the heat uptake. An increase in heat source power is like a decrease in

welding speed leading to an increase in heat input per unit length. This effect is also depicted in Figures 6(b) and 6(c).

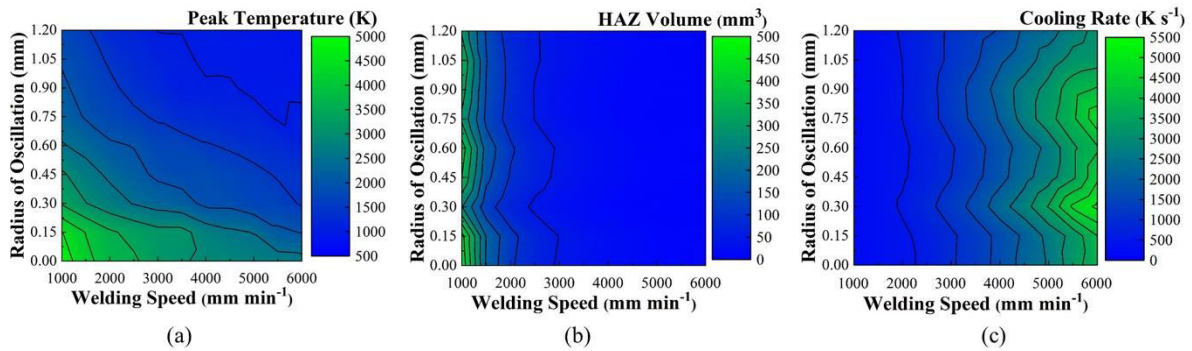


Fig. 8 Parametric contour map for the radius of oscillation vs welding speed at a constant power of 4000 W and frequency of oscillation of 200 Hz. Figure (a) shows a contour map for peak temperature, (b) shows HAZ volume, and (c) shows for cooling rate. The parametric contour maps are developed for the joining of Al-5754 with the Al-6061 alloy system for butt welding configuration.

3.3.3 Effect of beam oscillation on the process capability space

From section 3.3.1, it was concluded that the effect of the frequency of oscillation is negligible on the IPIs for the range of frequencies investigated in this study. So, the Pc-space depends on only three process parameters yielding a 3D response surface, where x , y , and z axes are the three process parameters which are heat source power, welding speed and radius of oscillation respectively. This response surface can be visualized by stacking up 2D contour plots in the xy plane with a constant value for the third process parameters, as shown in figure 9. The size of the Pc-space increases and is applicable for broader process parameter ranges with increasing radius of oscillation as depicted in Figure 9. This demonstrates the increase in flexibility of the laser welding process due to the application of beam oscillation. The upper limit of the allowed peak temperature ceases to exist at the highest radius of oscillation as shown in Figure 9 (f). For the same combination of welding speed and heat source power, the peak temperature decreases though the net heat input to the workpiece is the same when compared to the non-oscillating heat source. To attain the same peak temperature oscillating heat source requires more heat input as compared to a non-oscillating condition which is shown in Figure 9(a) and 9(b) where to achieve the upper limit of peak temperature of 3500 K in oscillation condition requires more power at the same welding speed.

3.4 Process capability space refinement

Process capability space refinement is illustrated by using the example of improving mechanical properties for the keyhole-mode of welding for full penetration. In this example, the final process capability space is chosen for no oscillation condition which is illustrated in Figure 10(a). The region above the feasible region (marked yellow) corresponds to the cutting or over weld region as this region causes burn-through due to deeper penetration of the keyhole. The region below the feasible region depicts the under-weld region where due to insufficient penetration leads to a poor coalition of the materials. The last region at the bottom is no welding region/ preheating as the peak temperature is below the melting point of the material. The first step for process capability space refinement depending upon the downstream process requirement is to select the proper peak temperature thus satisfying IPIs constraints as given in Table 3. The lower limit of peak temperature should be greater than the boiling point of the metal as keyhole-mode of welding is considered, and the upper limit should be less than 3500 K (as this temperature corresponds to full penetration welding). The yellow-coloured region in Figure 10(b) represents a feasible region for the keyhole mode of welding. The region just below the feasible region (in between the red and black lines) represents the feasible region for the conduction mode of welding. In the second step, the WPPs combinations are narrowed down based on the objective functions (Table 3) which are minimising HAZ volume and maximising cooling rate. The narrowed down process capability space based on the objective function is shown in Figure 10(c). In the final step, those process parameter combinations are selected from the refined space which has faster welding speed and lower heat source power (WPPs constraints as given in Table 3). For a special case of full penetration keyhole welding, the peak temperature should be 3500 K, so the refined process capability space is just a line in place of an area as shown in Figure 10(d). Therefore, the final refined process capability space has the full penetration welding with the lowest HAZ volume, highest cooling rate, highest welding speed, and lowest power. The robust process parameters can be selected from the refined process capability space having initial estimates about the quality of the weld from the IPIs without prior experimental characterization and mechanical testing. This approach reduces the number of experiments required. A similar approach can be used for the conduction mode of welding where the peak temperature should be less than the boiling point of the materials.

3.5 Surrogate for the quick estimation of peak temperature

The frequency of oscillation has a negligible effect on the IPIs as concluded in section 3.3.1 from the parametric contour maps. Therefore, regression analysis is only performed for

welding speed (S), heat source power (P) and radius of oscillation (R) as independent variables. Peak temperature, cooling rate and HAZ volume are evaluated as outcomes (IPIs) depending upon the goodness of fit. The adequacy of the surrogate model and the significance of the coefficients are analysed using the sequential analysis of variance (ANOVA). The codes are written in the Python programming language. A 10-Fold Cross Validation is performed to check the robustness of the model. In this method, fitting is performed ten times, with each fit being performed on a training set which consists of 90% of the total training set selected randomly, with the remaining 10% used as a holdout set for validation. The ANOVA provides which process parameters significantly affect each IPIs. Table 4 presents the analysis-of-variance of the responses (peak temperature, cooling rate and HAZ volume) and provides the F-value, p-value, percentage of contribution (POC), R-square, adjusted R-square and 10-Fold R-square. At 95% confidence interval, a p-value greater than 0.05 is statistically insignificant and a p-value less than or equal to 0.05 is statistically significant. The second-order and third-order polynomial equation was exploited to formulate the thermal responses as defined in equation (8). The number of data points taken to perform multivariate regression analysis was more than 700 following the criteria suggested by Green [39]. For the peak temperature and cooling rate quadratic polynomial equation was used while for HAZ volume cubic polynomial equation was used. The R-square, adjusted R-square and 10-Fold R-square for all the responses are greater than 90% which shows that the model is reasonable and effective. The results from ANOVA for the peak temperature, the laser power (POC = 52.7%) and the radius of oscillation (POC = 19.2%) are the most significant model term. Secondly, for the cooling rate welding speed (POC = 47%) and laser power (POC = 20.3%) are the most significant term (POC = 47%). Finally, for the cooling rate, welding speed (POC = 43.3%) and the interaction effect of laser power and welding speed (P*S having POC = 15.3%) are the most significant terms.

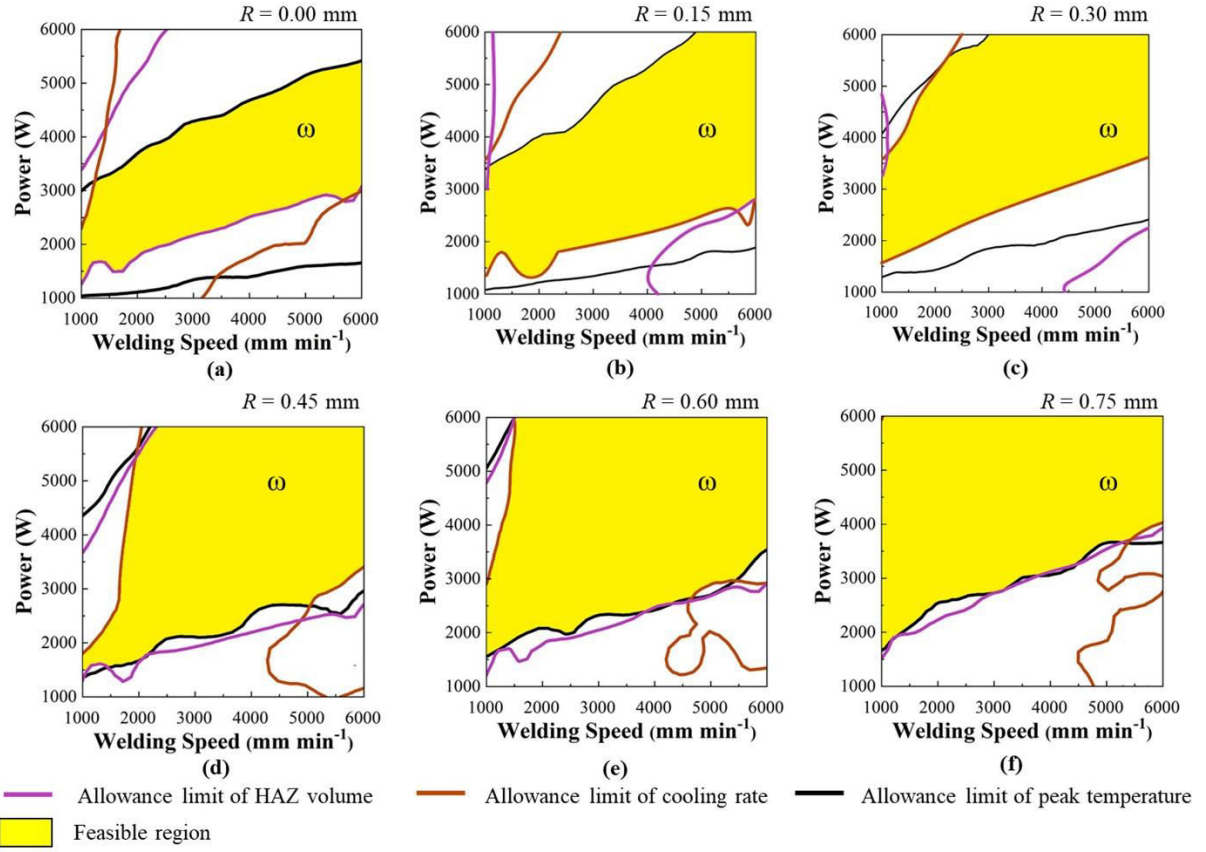


Fig. 9 Showing the process capability space for three process parameters to show 3D response surface as a stacked up 2D contour map. The z-axis for the 3D response surface is radius of oscillation which is varied at (a) $R = 0$ mm, (b) $R = 0.15$ mm, (c) $R = 0.30$ mm, (d) $R = 0.45$ mm, (e) $R = 0.60$ mm and (f) $R = 0.75$ mm in the 2D contour maps at a constant frequency of 300 Hz.

The surrogate model for the thermal responses (Eqs. 18-20), used for the prediction within the process capability space and design space in terms of process parameters are shown below:

$$T_{peak} = 759.9 - 1695 \times R + 1.1 \times P - 0.4 \times S + 1590 \times R^2 + 1.5 \times 10^{-5} \times P^2 + 5.1 \times 10^{-5} \times S^2 - 7.337 \times 10^{-1} \times R \times P + 2.660 \times 10^{-1} \times R \times S - 1.01 \times 10^{-4} \times P \times S \quad (18)$$

$$C_{rate} = 2949 - 816 \times R - 2.418 \times P + 2.2035 \times S - 299 \times R^2 + 3.55 \times 10^{-4} \times P^2 + 9.9 \times 10^{-5} \times S^2 + 3.856 \times 10^{-1} \times R \times P - 7.81 \times 10^{-2} \times R \times S - 4.60 \times 10^{-4} \times P \times S \quad (19)$$

$$V_{HAZ} = 78 - 186 \times R + 6.6 \times 10^{-2} \times P - 1.788 \times 10^{-1} \times S + 523 \times R^2 + 4.1 \times 10^{-5} \times P^2 + 1.02 \times 10^{-4} \times S^2 - 1.970 \times 10^{-1} \times R \times P + 2.989 \times 10^{-1} \times R \times S - 1.06 \times$$

$$10^{-4} \times P \times S - 579 \times R^3 + 1.511 \times 10^{-1} \times R^2 \times P - 1.313 \times 10^{-1} \times R^2 \times S + 3 \times 10^{-6} \times R \times P^2 - 2.2 \times 10^{-5} \times R \times S^2 \quad (20)$$

Figure 11 a-c shows the dispersion plots representing the relationship between the numerical (from the FEM model) and predicted values (from the surrogate model) of T_{peak} , V_{HAZ} and C_{rate} with a 95% confidence level. These dispersion plots indicate the accuracy and adequacy of the model developed and the predicted results are in good agreement with the measured data.

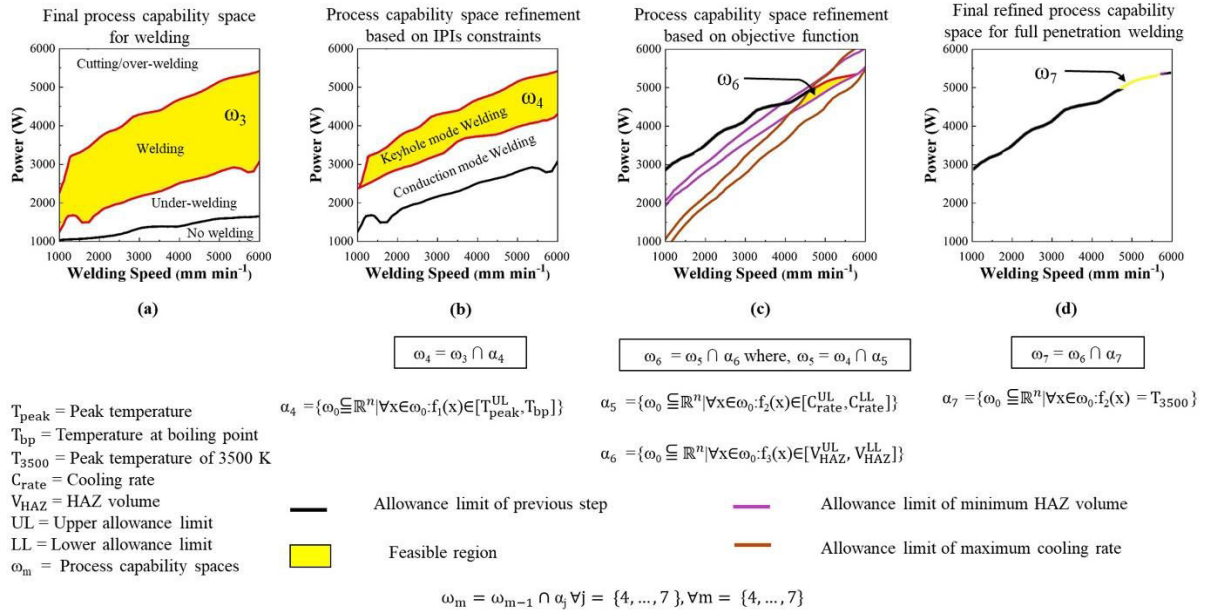


Fig. 10 (a) Final process capability space for welding having cutting/over-welding region, welding region, under-welding region and no-welding/pre-heating region (b) Process capability space refinement based on IPIs constraints i.e. $3500 \text{ K} \geq T_{\text{peak}} > T_{\text{bp}}$ having cutting/over-welding region, keyhole mode welding region, conduction mode welding region and under-welding region ; (c) Process capability space refinement based on the objective functions i.e. minimising HAZ volume and maximising cooling rate and (d) Final refined process capability space for full penetration welding. The temperature 3500 K shows the estimated peak temperature for full penetration welding.

3.5.1 Effect of input process parameters on responses

The response profilers for the effect of process parameters on the thermal responses have been constructed according to the surrogate models (Eqs. 17-19). Figure 12 shows the prediction profiler for the responses (T_{peak} , V_{HAZ} and C_{rate}) for oscillation and no oscillation condition with the variables within the working range. The surrogate model have similar trends as shown by the FEM simulations with respect to the responses due to the variation in

process parameters as shown in Figure 12. Beam oscillation has a cyclic effect on the HAZ volume and cooling rate as shown in Figures 12 (f) and (i). It is due to the two competing factors. The heat is distributed in a larger area i.e., the heat input decreases leading to shallow penetration leading to a decrease in HAZ volume but on the other hand, a larger radius leads to a wider melt pool, thus increasing HAZ volume. Similarly for the cooling rate reheating leads to a decrease in cooling rate while due to larger area interaction heat input per unit length decreases leads to an increase in cooling rate. Beam oscillation will always yield lower peak temperature, HAZ volume for the same process parameters combination. While for the cooling rate the application of beam oscillation may decrease or increase the cooling rate depending upon the two competing factors.

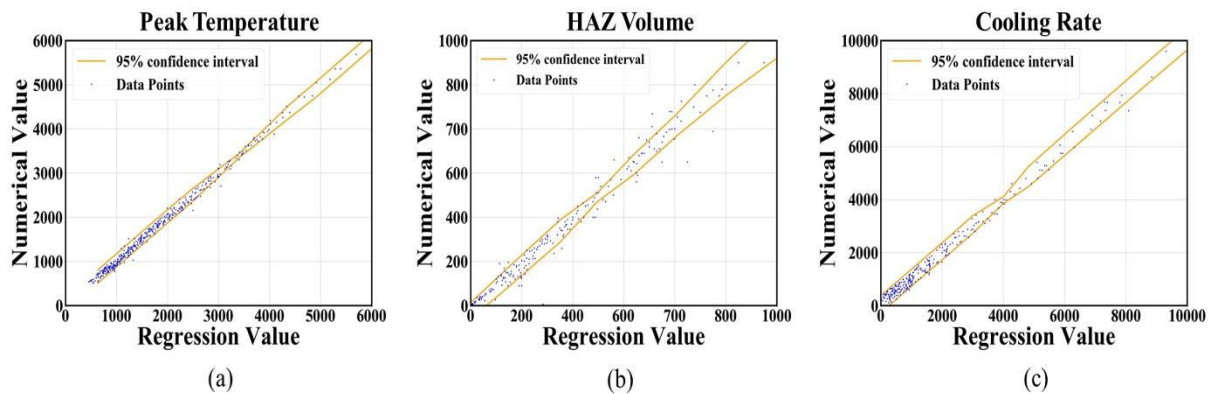


Fig. 11 Value of the peak temperature, HAZ volume and cooling rate from the FEM model vs predicted from the surrogate model with a 95% confidence interval to show the accuracy of the polynomial fit function. The dispersion plot was developed for the joining of Al-5754 with the Al-6061 alloy system for butt welding configuration using 740 data points extracted from the physics-based model.

In Pc-space of peak temperature, the combination of the three main welding parameters (welding speed, heat source power, and radius of oscillation) will form a plane in 3D design space representing a specific peak temperature and each point on that plane will give the welding process parameters combination to attain the required peak temperature. It provides ternary interactions (showing the interactions of all the process parameters at once) of process parameters for the development of Pc-space as compared to the parametric contour maps which depend on the binary interactions of WPPs (showing interactions of two process parameters at a time and keeping the rest constant). The Pc-space depicted by contour maps shows the peak temperature for all possible ranges of process parameters. But, in the case of

the surrogate model, the Pc-space shows all the possible WPPs combinations for a particular peak temperature.

Table 4 ANOVA for the surrogate for different responses.

ANOVA Terms	Responses								
	Peak Temperature			Cooling Rate			HAZ Volume		
Source	F-value	p-value	POC	F-value	p-value	POC	F-value	p-value	POC
Model	4628.9	0.000	98.3	1002.3	0.000	94.3	265.1	0.000	92.04
R	227.3	0.000	19.2	3.7	0.054	3.2	0.4	0.493	0.3
P	2475.7	0.000	52.7	484.5	0.000	20.3	0.2	0.630	10.9
S	331.6	0.000	14.4	769.1	0.000	47.0	7	0.008	43.3
R ²	216	0.000	0.5	0.5	0.451	0.0	1.6	0.201	0.2
P ²	28.5	0.000	0.0	588.4	0.000	3.8	1.2	0.261	0.1
S ²	343.2	0.000	0.8	104	0.000	0.3	55.1	0.000	10.9
R*P	2397.9	0.000	5.6	24.4	0.000	1.3	3.8	0.049	0.2
R*S	315.1	0.000	0.7	1.8	0.170	1.4	35.9	0.000	0.7
P*S	1732.5	0.000	4.1	1607	0.000	16.8	13.7	0.000	15.3
R ³	-	-	-	-	-	-	4	0.044	0.05
P ³	-	-	-	-	-	-	0.7	0.391	0.01
S ³	-	-	-	-	-	-	329.7	0.000	3.2
R ² *P	-	-	-	-	-	-	6.9	0.009	0.05
R ² *S	-	-	-	-	-	-	10.9	0.001	0.2
P ² *R	-	-	-	-	-	-	0.07	0.796	0.0
S ² *R	-	-	-	-	-	-	13.9	0.000	0.3
P ² *S	-	-	-	-	-	-	31.1	0.000	0.6
S ² *P	-	-	-	-	-	-	277.9	0.000	5.3
R-sq	98.31 %			94.37 %			92 %		
R-sq(adj)	98.29 %			94.28 %			91.6 %		
10-Fold R-sq	98.25 %			93.96 %			90.8 %		

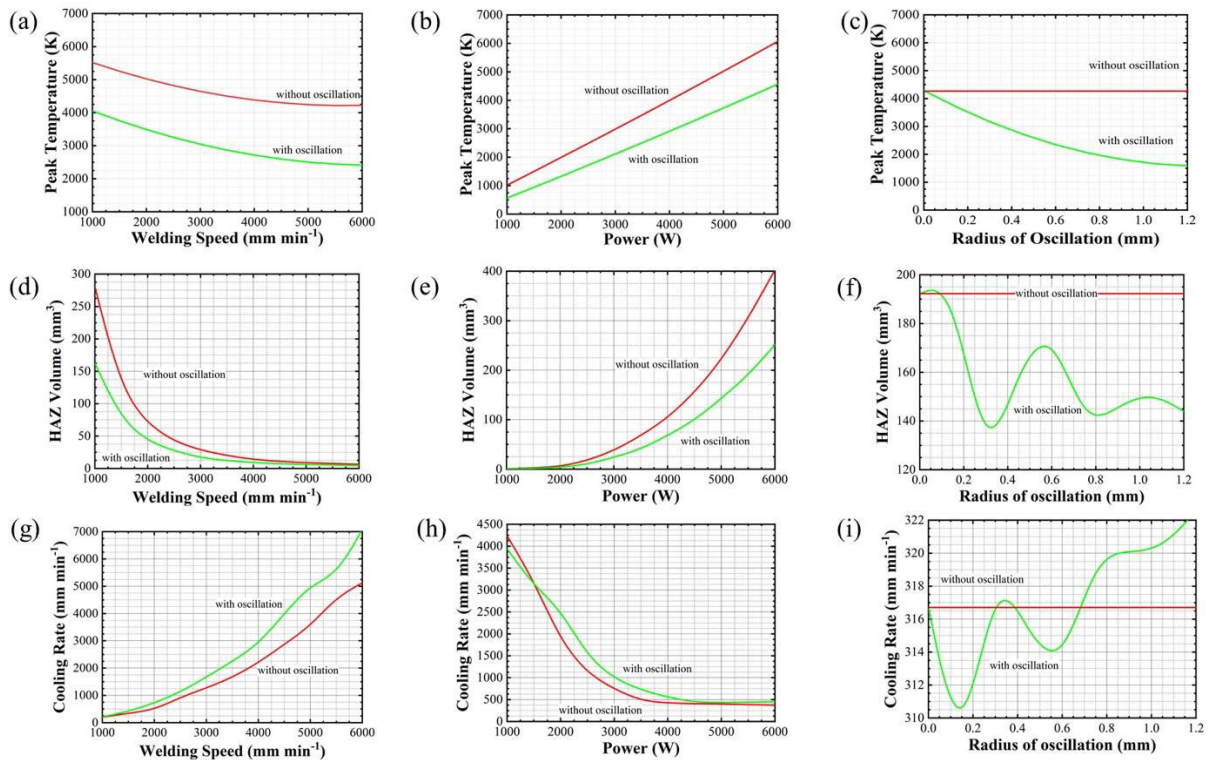


Fig. 12 Peak temperature (a-c), HAZ Volume (d-f) and cooling rate (g-i) prediction profiler to depict the relationship between the welding process parameters and the thermal responses and also to depict the linear/non-linear dependency between them.

Therefore, it provides a finer grid in the Pc-space as compared to the parametric contour plots. This is a more general and robust approach as compared to the binary interactions shown with the parametric contour maps. The 3D graph generated will save time from running many simulations and shows the effect of the three process parameters at once, unlike the contour maps where the effect can be understood for two parameters at a time. One example is shown in Figure 13 where the required peak temperature is set to 2500 K. The red line shows the solution for without oscillation. The 3D graph gives a better visualization of the equivalent effect of process parameters and the flexibility of the laser welding process.

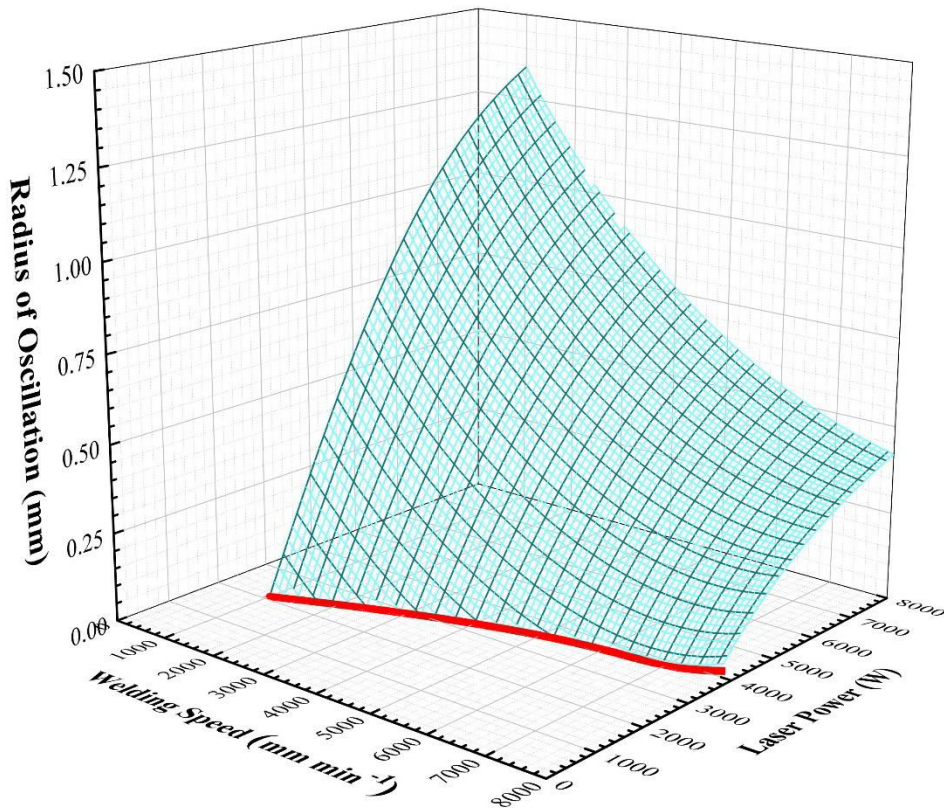


Fig. 13 Response surface generated from the regression model for the effect of welding speed, the radius of oscillation, and heat source power for a peak temperature of 2500 K. The red line shows the response surface for no oscillation conditions. The response surface is developed for the joining of Al-5754 with an Al-6061 alloy system for butt welding configuration.

4. Conclusions

This paper presents a novel methodology for the process capability space refinement for the laser welding process. During this research, FEM based heat transfer model has been developed to simulate the peak temperature, HAZ volume and cooling rate in laser welding. Process capability space has been depicted by using parametric contour maps. A semi-empirical mathematical model was developed and validated. The main conclusions are as follows:

- There is a good agreement between the FEM model and the experiments both in terms of thermal cycle and weld morphology to evaluate thermal responses.
- It has been found that the welding speed and heat source power has an opposite effect on the IPIs.

- Parametric contour maps show that the effect of oscillation frequency is negligible on the IPIs during beam oscillation. The main parameter affecting the weld thermal cycle during beam oscillation is the radius of oscillation.
- The final process capability space increases with the application of beam oscillation which exhibits the increase in flexibilities due to beam oscillation.
- Application of beam oscillation always decreases the peak temperature and HAZ volume while it may increase or decrease the cooling rate.
- The cooling rate and HAZ volume varies cyclically with the change in radius of oscillation.

Finally, it should be stressed that the presented modelling approach, relies on the thermal aspect of the welding only and all the calculation is based on temperature. Nevertheless, the main features are likely to represent the experimental situation sufficiently for the IPIs studied, especially parametric study for the interdependency of the process parameters for the target welding quantities (IPIs), assessment of the sensitivity of process parameters on the IPIs, and the process capability space refinement for the design of the experiments. The presented approach is general in its nature and can be applied to other welding techniques as it models heat source and heat transfer during welding which is fundamental for every welding technique. Further, the present model can also be used for parameter selection where partial penetration is required or the temperature at the bottom surface must not exceed a particular temperature such as joining battery tabs during battery pack assembly.

Acknowledgements

This work is supported by the WMG, University of Warwick (United Kingdom), and the Indian Institute of Technology Kharagpur (India) as the financial support for the PhD studentship via the WMG-IIT partnership program.

Author Contribution Anand Mohan contributed to the conceptualization, defined methodology, developed the numerical model, performed experiment for validation, and formal analysis and manuscript preparation. Dariusz Ceglarek and Michael Auinger contributed to supervision, and manuscript writing, review and editing.

Declarations

Conflict of interest The author declare no competing interests.

Ethics approval Not applicable.

Consent to participate Not applicable.

Consent for publication Not applicable.

References:

1. Rietmann N, Lieven T (2019) How policy measures succeeded to promote electric mobility – Worldwide review and outlook. *J Clean Prod* 206:66–75
2. González PJC, Furubayashi T, Nakata T (2012) Energy use and CO2 emissions reduction potential in passenger car fleet using zero emission vehicles and lightweight materials. *Energy* 48:548–565
3. Seffer O, Pfeifer R, Springer A, Kaielerle S (2016) Investigations on laser beam welding of different dissimilar joints of steel and aluminum alloys for automotive lightweight construction. *Phys Procedia* 83:383–395
4. Pardal G, Mecco S, Dunn A, et al (2017) Laser spot welding of laser textured steel to aluminium. *J Mater Process Technol* 241:24–35
5. Ceglarek D, Colledani M, Vánicza J, et al (2015) Rapid deployment of remote laser welding processes in automotive assembly systems. *CIRP Ann. - Manuf. Technol.* 64:389–394
6. Mahamood RM, Akinlabi ET (2018) Non-contact Welding Technologies: Fusion Welding. In: *Advanced Noncontact Cutting and Joining Technologies*. Springer Cham, 139–165
7. Kuryntsev S V, Gilmutdinov AK (2015) The effect of laser beam wobbling mode in welding process for structural steels. *Int J Adv Manuf Technol* 81:1683–1691
8. Kraetzsch M, Standfuss J, Klotzbach A, et al (2011) Laser beam welding with high-frequency beam oscillation: Welding of dissimilar materials with brilliant fiber lasers. *Phys Procedia* 12:142–149
9. Vemanaboina H, Edison G, Buddu RK (2018) Thermal Analysis Simulation for Laser Butt Welding of Inconel625 Using FEA. *Int J Eng Technol* 4:85–89
10. Dal M, Fabbro R (2016) An overview of the state of art in laser welding simulation. *Opt Laser Technol* 78:2–14

11. He X (2012) Finite element analysis of laser welding: A state of art review. *Mater Manuf Process* 27:1354–1365
12. Wang Z, Oliveira JP, Zeng Z, et al (2019) Laser beam oscillating welding of 5A06 aluminum alloys: Microstructure, porosity and mechanical properties. *Opt Laser Technol* 111:58–65
13. Rosenthal D (1941) Mathematical theory of heat distribution during welding and cutting. *Weld J* 20:220–234
14. Rosenthal D (1946) The Theory of Moving Source of Heat and it's Application to Metal Treatment. *Trans ASME* 849–866
15. Swift-Hook DT, Gick AEF (1973) Penetration Welding with Lasers. *Weld Res Suppl* 492–499
16. Lax M (1977) Temperature rise induced by a laser beam. *J Appl Phys* 48:3919–3924
17. Dowden J (1983) Some aspects of the fluid dynamics of laser welding. *J Fluid Mech* 126:123–146
18. Goldak J, Chakravarti A, Bibby M (1984) A new finite element model for welding heat sources. *Metall Trans B* 15:299–305
19. Chukkan RJ, Vasudevan M, Muthukumaran S, Kumar RR (2015) Simulation of laser butt welding of AISI 316L stainless steel sheet using various heat sources and experimental validation. *J Mater Process Tech* 219:48–59
20. Jin X, Li L (2004) An experimental study on the keyhole shapes in laser deep penetration welding. *Opt Lasers Eng* 41:779–790
21. Spina R, Tricarico L, Basile G, Sibillano T (2007) Thermo-mechanical modeling of laser welding of AA5083 sheets. *J Mater Process Tech* 191:215–219
22. Nguyen N., Ohta A, Matsuoka K, et al (1999) Analytical Solutions for Transient Temperature of Semi-Infinite Body Subjected to 3-D Moving Heat Sources. *Weld Res Suppl* 265–274
23. Little GH, Kamtekar AG (1998) The effect of thermal properties and weld efficiency on transient temperatures during welding. *Comput Struct* 68:157–165
24. Hou ZB, Komanduri R (2000) General solutions for stationary/moving plane heat

- source problems in manufacturing and tribology. *Int J Heat Mass Transf* 43:1679–1698
25. Gutierrez G, Araya JG (2003) Temperature Distribution in a Finite Solid Due to a Moving Laser Beam. *Int Mech Eng Congr R&D Expo* 3:259–271
 26. Bianco N, Manca O, Nardini S, Tamburino S (2008) Transient Heat Conduction in Solids Irradiated by a Moving Heat Source. In: *Defect and Diffusion Forum*. pp 358–363
 27. Shanmugam NS, Buvanashakaran G, Sankaranarayanan K, Ramesh Kumar S (2010) A transient finite element simulation of the temperature and bead profiles of T-joint laser welds. *Mater Des* 31:4528–4542
 28. Shanmugam NS, Buvanashakaran G, Sankaranarayanan K (2013) Some studies on temperature distribution modeling of laser butt welding of AISI 304 stainless steel sheets. *World Acad Sci Eng Technol* 7:1532–1541
 29. Tsirkas SA, Papanikos P, Kermanidis T (2003) Numerical simulation of the laser welding process in butt-joint specimens. *J Mater Process Technol* 134:59–69
 30. Ozkat EC, Franciosa P, Ceglarek D (2017) Development of decoupled multi-physics simulation for laser lap welding considering part-to-part gap. *J Laser Appl* 29:022423
 31. D'Ostuni S, Leo P, Casalino G (2017) FEM Simulation of Dissimilar Aluminum Titanium Fiber Laser Welding Using 2D and 3D Gaussian Heat Sources. *Metals* 7:1–15
 32. Atabaki MM, Nikodinovski M, Chenier P, et al (2014) Experimental and numerical investigations of hybrid laser arc welding of aluminum alloys in the thick T-joint configuration. *Opt Laser Technol* 59:68–92
 33. Rahman J, Vasudevan M, Muthukumaran S, Kumar RR (2015) Simulation of laser butt welding of AISI 316L stainless steel sheet using various heat sources and experimental validation. *J Mater Process Tech* 219:48–59
 34. Abderrazak K, Bannour S, Mhiri H, et al (2009) Numerical and experimental study of molten pool formation during continuous laser welding of AZ91 magnesium alloy. *Comput Mater Sci* 44:858–866
 35. Wang L, Gao M, Zhang C, Zeng X (2016) Effect of beam oscillating pattern on weld

- characterization of laser welding of AA6061-T6 aluminum alloy. *Mater Des* 108:707–717
36. Fetzner F, Sommer M, Weber R, et al (2018) Reduction of pores by means of laser beam oscillation during remote welding of AlMgSi. *Opt Lasers Eng* 108:68–77
 37. Bramson MA (1968) *Infrared Radiation: A Handbook for Applications*. Plenum Press, New York
 38. Shi Q, Gu D, Xia M, et al (2016) Effects of laser processing parameters on thermal behavior and melting/solidification mechanism during selective laser melting of TiC/Inconel 718 composites. *Opt Laser Technol* 84:9–22
 39. Green SB (1991) How many subjects does it take to do a regression analysis. *Multivariate Behav Res* 26:499–510
 40. Seli H, Awang M, Ismail AIM, et al (2013) Evaluation of properties and FEM model of the friction welded mild steel-Al6061-alumina. *Mater Res* 16:453–467

Appendices

Appendix A: Thermo-physical properties of the alloys

Table A.1 Thermo-physical properties of AA5754, Ti6Al4V and Al-6061 alloys used in this study [31, 40].

Property	AA5754	Ti6Al4V	Al-6061
Density (g cm ⁻³)	2.7	4.4	2.68
Liquidus Temperature (K)	870	1923	925
Solidus Temperature (K)	856	1880	855

Table A.2 Temperature-dependent thermal conductivity value for alloys AA5754, Ti6Al4V and Al-6061 used in this study [31, 40].

Thermal Conductivity (W m ⁻¹ K ⁻¹)			
Temperature (K)	AA5754	Ti6Al4V	Al-6061
293	138	6.01	162
373	147.2	7.1	177
473	152.7	8.5	192
573	162.7	9.4	207

673	152.7	11.3	216
773	158.75	14.78	223
873	138	17.20	253
1773	138	34.3	253

Appendix B: Calculation of energy input per unit length (in one revolution) vs frequency of oscillation

For the range of welding speed (S), radius of oscillation (R) and frequency of oscillation (f) investigated in this study, the shape of oscillation is considered circular for calculating the number of overlapping points and the length traversed by the heat source in one revolution. To calculate the energy input per unit length, energy input is considered as 1 J s^{-1} length of the curve in revolution is calculated by the line integration from zero to $(1/f)$ seconds and the number of overlapping points in one revolution is calculated graphically in terms of process variables. $(1/f)$ is the time taken to complete one revolution.

B.1 Derivation of the condition for the onset of overlapping

Trajectory equation for the position of oscillating heat source in xy -plane as z -component remains constant taken from the Eq. (4)

$$P(x(t), y(t)) = \left(x_0 + St - R(1 - \cos(2\pi ft)), y_0 + R\sin(2\pi ft) \right) \quad (\text{B.1})$$

For the onset of overlapping the position of the heat source in the y -axis should be R (using the negative sign for negative y -direction) as shown in Figure 14.(a) and the time taken is t_1 ,

$$y(t_1) = -R \quad (\text{B.2})$$

Putting equation (B.2) in equation (B.1) gives,

$$y_0 + R\sin(2\pi ft_1) = -R \quad (\text{B.3})$$

Considering the initial position of the heat source at origin ($y_0 = 0$) gives

$$t_1 = \frac{3}{4f} \quad (\text{B.4})$$

Now, at the onset of overlapping the position of heat source in the x -direction at time t_1 should be $2R$

$$x(t_1) = 2R \quad (\text{B.5})$$

$$x_0 + St_1 - R(1 - \cos(2\pi ft_1)) = 2R \quad (\text{B.6})$$

Putting $t_1 = \frac{3}{4f}$ in equation (B.6)

$$\text{Which gives,} \quad S = 4Rf \quad (\text{B.7})$$

Equation (B.7) gives the condition for the onset of the overlapping. Welding speed greater than this value will have no overlapping points.

B.2 Estimation of overlapping points graphically

The number of overlapping points is estimated graphically in terms of welding speed, radius of oscillation and frequency of oscillation due to the complexity of equations. The graphical solution comprises plotting and counting the number of overlapping points in terms of process variables and finding the general series as given in Table B.1. Using general induction of $S = (4/(2n+1))Rf$ and adding two more overlapping points for each cross-over. Graphical solutions yield the number of overlapping points as a function welding speed radius of oscillation and frequency of oscillation which is given in Table B.1. Just to note that this relationship has been proved by the method of induction.

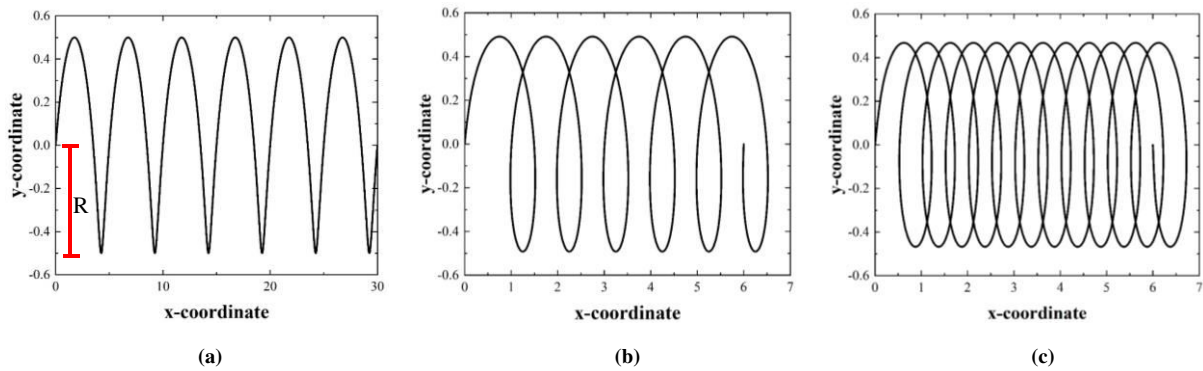


Fig. 14 Showing trajectory of beam oscillation for (a) No overlapping and the onset of overlapping when $S \geq 4Rf$, (b) overlapping at a lower frequency of oscillation when $S \leq 4Rf$; and (c) overlapping at a higher frequency of oscillation when $S \leq 4Rf$.

B.3 Energy input per unit length

The distance travelled by the heat source in one revolution is calculated by Eq. (B.8)

$$l = \int_0^{1/f} \sqrt{v^2 + (2\pi Rf)^2 + (2\pi rfv \sin(2\pi ft))^2} dt \quad (\text{B.8})$$

So, total energy input per unit length (in one revolution) is given by Eq. (B.9)

$$E = \eta(T) \frac{P \times n}{l \times f} \quad (\text{B.9})$$

Where P is the power of the heat source, n is the number of overlapping points, l is the distance travelled by the heat source in one revolution, η is the absorption coefficient of material and f is the frequency which is also equal to the time taken for one revolution to take place.

Table B.1. Number of overlapping points with the condition associated with it depending on the radius of oscillation (R), frequency of oscillation (f) and welding speed (S).

Number of overlapping points	Condition
0	$S \geq 4Rf$
2	$4Rf > S > \frac{4}{3}Rf$
4	$S = \frac{4}{3}Rf$
6	$\frac{4}{3}Rf > S > \frac{4}{5}Rf$
$4n$	$S = \frac{4}{2n+1}Rf$
$4n+2$	$\frac{4}{2n+1}Rf > S > \frac{4}{2n+3}Rf$